Energy Engineering

Tech Science Press

https://doi.org/10.32604/ee.2026.083821

ARTICLE

Characterization of Bubble Dynamics in Nanofluid Flow under External Magnetic Field: Experimental and Numerical Approach

Hasanain A. Abdul Wahhab[1,*], Hamid Abdallah Dhaher[2], Miqdam T. Chaichan[3,4], Saif Ali Kadhim[5], Hayder Mohsin Ali[5], Muataz S. Alhassan[6] and Mohammed Fathi Muzahem[3]

[1]Training and Workshop Center, University of Technology-Iraq, Baghdad, Iraq
[2]The Manufacture of Cylinder Department, State Company for Gas Filling and Services, Ministry of Oil, Al Kut, Iraq
[3]Energy and Renewable Energies Technology Center, University of Technology-Iraq, Baghdad, Iraq
[4]Faculty of Engineering, Sohar University, Sohar, Oman
[5]Mechanical Engineering Department, University of Technology-Iraq, Baghdad, Iraq
[6]College of Engineering, Al-Ayen Iraqi University, Nasiriyah, Iraq

*Corresponding Author: Hasanain A. Abdul Wahhab. Email: 20085@uotechnology.edu.iq

Received: 11 April 2026; Accepted: 10 June 2026; Published: 06 August 2026

ABSTRACT: The magnetohydrodynamics of bubbly nanofluid flow in a horizontal pipe was studied. The drag-reduction effect of the behavior of a magnetohydrodynamic nanofluid in bubbly flow was experimentally verified by generating bubbles in the flow. The study examined the effects of the magnetic field on bubble formation by observing bubble characteristics, including shape, size, and trajectory. The experimental analysis adopted an optical system using a high-speed video camera. A MATLAB code was developed to track bubble formation in bubbly flow. The magnetic field affects the continuous nanofluid phase and, in turn, influences the gas phase and bubble features, such as bubble growth, shape, size, trajectory, and formation velocity. The results showed that under a magnetic field up to 4000 gauss and a nanofluid superficial velocity of 17.78 cm/s, the magnetic force had the greatest effect due to the increased electrical conductivity of the nanofluid. Also, in a magnetic field, bubble formation is delayed, leading to increased collisions and bubble merging. The magnetic field makes the bubble turbulent and unstable, especially after it separates from the nozzle tip, as evidenced by changes in its shape and trajectory. The shape factor of bubbles decreases as the magnetic field intensity increases. This effect is confirmed by the elongation of bubbles within the nanofluid flow.

KEYWORDS: Bubble production; nano technology; two-phase flow; magnetic field; Fe_3O_4

1 Introduction

Nanofluids are fluids in which nanoparticles are dispersed into base fluids, and due to their unique thermal characteristics and uses, they have captured the imagination of researchers from different disciplines. For instance, nanofluids enhance heat transfer in heat exchangers, and PCs used for electronic cooling; Al_2O_3 nanofluids increase heat sink effectiveness by 28.3% [1,2]. In renewable energy systems, they optimize solar collectors and improve the cooling systems of nuclear reactors, meaning that renewable energy systems can be safer and more efficient [3,4]. In the biomedical field, magnetic nanofluids are used in drug delivery systems and in thermally targeted cancer therapy via heat generation [5]. They are useful industrially as lubricants and coolants, especially in matching operations, since they reduce friction while enhancing finishes [6]. Furthermore, nanofluids have been shown to enhance heat transfer rates and reduce fouling on working surfaces during thermal desalination processes [7]. The examples above demonstrate the use of nanofluids and show that they are an essential focus of modern technological development. That they can bring about a marked enhancement in thermal efficiency across so many applications confirms the potential to change the face of many industries.

The significant enhancement of thermal conductivity and heat transfer in fluids using nanomaterials, under the influence of a sufficiently strong magnetic field, is possible [8]. For instance, when magnetic nanoparticles are dispersed in a base fluid, applying a magnetic field aligns them into a chain that serves as a path for heat transport. It also enhances thermal conduction and convective heat transfer rates [9]. The investigations in the current literature also confirm that a magnetic field facilitates the formation of these structures and can enhance the heat transfer coefficients of nanofluids by up to 30 percent or more [10]. In addition, the dispersion process using ultrasound helps distribute nanoparticles uniformly throughout the fluid—a factor that significantly bolsters the potential of these thermal upgrades. In addition to enhancing the thermal properties of nanofluids, magnetic field absorption, along with ultrasound treatment, improves energy conversion in applications such as electronic cooling and cooling systems in renewable energy systems [11].

Magnetic nanoparticles in a nanofluid are heated primarily by hysteresis and Néel losses when an alternating current is passed through an immersed coil [12]. The energy loss arises from the magnetization retardation of the metallic nanoparticles in response to variations in the applied magnetic field, which converts energy into heat. Similarly, Néel losses occur from the magnetization process of the nanoparticles when they are aligned with the modified magnetic field [13]. This process not only contributes to heat production within the nanoparticles but also enhances heat exchange with the surrounding core fluid. When the nanoparticles are heated, they transfer heat to the core fluid, thereby increasing its temperature. This mechanism is very useful in cases of high heat flow from a heat-carrying fluid to a heat sink, for example, for cooling electronic modules or in thermal systems handling industrial processes. The performance of this heating mechanism can be significantly improved if the above parameters of the MNPs, such as their concentration and size, as well as the frequency and amplitude of the AC current, are well controlled.

Studies have shown that increasing nanoparticle concentrations enhances hysteresis losses, thereby increasing the overall heat capacity of the nanofluid. Furthermore, smaller nanoparticles have a higher surface-to-volume ratio, which can be beneficial for the base fluid and improve thermal conductivity [14]. This is because the combined effects of these factors are essential for achieving the highest possible heat transfer rates in practical applications. However, the addition of a magnetic field within the system can induce secondary flows in the nanofluid, thereby enhancing convective heat transfer [15]. In addition to nano-alignment, the application of a magnetic field also drives particles through the fluid, further improving dynamic mixing and heat transfer [16]. Analytical and experimental investigations have shown that an integrated approach yields significant improvements in thermal performance, with heat transfer coefficients increasing by 13% to 75% depending on flow conditions [17–20].

A quite challenging and interesting discussion can be held on the behavior of collapsing bubbles and the associated effects in high-thermal-conductivity nanofluids, with a focus on magnetic-field effects at gas/liquid interfaces [21]. When a gas bubble forms in a nanofluid, for instance, a magnetic particle nanofluid, the coupling between thermal conductivity and external magnetic fields greatly influences the bubble's behavior during collapse [22]. It is established from the existing literature that, when an external magnetic field is applied, the thermal conductivity of the nanofluid increases, which in turn influences the temperature and pressure within the bubble [23].

Even in cavitation cases, the pressure change is dramatic during bubble collapse, and inside the bubble, conditions are extreme. This process is characterized by a rapid compression phase in which the temperature can soar due to adiabatic compression [24]. The exaltation of this effect is due to magnetic nanoparticles, which, when subjected to a magnetic field, exhibit hysteresis and Néel losses that produce heat. It is conducted to the surrounding fluid, causing changes in temperature and the thermophysical properties of the nanofluid [25]. As a result, the thermal conductivity coefficient enhances heat transfer from the nanoparticles to the base fluid during bubble-collapse energy dynamics. In their work, when the bubble shrinks, the investigations show that the vapor temperature can exceed that of the surrounding fluid [26]. The local heat sources that are created by the oscillating bubble's interaction with the magnetic field make the fluid behavior highly nonlinear, which is due to the combined thermal and hydrodynamic forces at play. For example, situations in which bubbles collapse near solid walls or in confined volumes are even more extraordinary. As for the post-collapse stage, the nature of the curved surface may affect the development of secondary collapse or oscillations, thereby improving heat transfer characteristics [27–30]. Furthermore, this has practical significance for other engineering applications, such as the improvement of heat exchangers or cooling systems for electronic equipment [31]. Exciting for thermal management is the prospect offered by the work, the possibility of controlling the bubble dynamics via magnetic fields. Since these effects depend on variables such as nanoparticle concentration, magnetic field strength, and fluid properties, engineers can manipulate these parameters to leverage the effects and improve the system [32]. In some cases, one can use computations and simulations to predict how bubbles will behave under different conditions in experimental setups. For example, lattice Boltzmann methods have been applied to model cavitation processes and to examine the effects of bubble dynamics on heat transfer in nanofluids. In these cases, the augmentation of the convective heat transfer coefficient by nanoparticles appears to be substantiated when a high nanoparticle concentration or an optimal magnetic field strength is applied to the fluids [33–37].

In conclusion, the ways in which bubbles in high-thermal-conductivity nanofluids are destroyed by a magnetic field is an interesting area of study that falls within the domains of thermophysics, fluid dynamics, and magnetism. The magneto-mechanical characteristics of magnetic nanoparticles for heat generation not only influence bubble dynamics but also enhance thermal conductivity and heat transfer coefficients. While research on these interactions is ongoing, it has revealed the potential to improve these technologies across areas such as energy, biomedical, and materials. Knowledge of these mechanisms would be essential to the development of new solutions that effectively leverage nanofluid properties in real-world scenarios. This work was to investigate the enhancement of water magnetization with iron oxide Fe_3O_4 nanoparticles at a laminar flow of nanofluid and the treatment of this flow with the effect of the magnetic field, especially, which might implement the use of magneto-hydrodynamic MHD control on the bubbly flow characteristics to be applied for the enhancement of injection systems into production processes.

The novelty of this work lies in its integrated experimental and numerical investigation of magnetohydrodynamic (MHD) effects on bubbly nanofluid flow, a topic with limited direct experimental validation in the literature. Unlike conventional studies that examine nanofluids or bubbly flows separately, the present study combines both phases under controlled magnetic fields to reveal coupled interfacial dynamics. A high-speed optical imaging system, together with a custom MATLAB-based tracking algorithm, was employed to provide quantitative and time-resolved characterization of bubble formation, growth, deformation, and motion. In addition, delayed bubble detachment, enhanced coalescence, increased instability, and measurable variations in the bubble shape factor were experimentally and numerically demonstrated as the magnetic field intensity increased. The numerical model successfully reproduced the main experimental trends, including bubble elongation, size increase, and migration patterns, confirming the reliability of the coupled multiphase MHD analysis. These findings provide new physical insight into phase interactions in MHD environments and contribute toward improving transport phenomena in advanced cooling and energy-related applications.

2 Experimental Implementation

The experimental setup for the bubbly nanofluid flow in a horizontal pipe is schematically depicted in Fig. 1a. In this experiment, the optical approach was utilized. Thus, the test section was made of clear polycarbonate. The test part is 0.05 m in diameter and 0.8 m in length. The purpose of the air injection device installed at the beginning of the test section was to create air bubbles inside the test segment. The air injection system was connected to the tiny compressed air line and the nanofluid line. The Fe_3O_4–water nanofluids were prepared at a volume fraction 0.5% by dispersing Fe_3O_4 nanoparticles in deionized water. Initially, the mixture was stirred magnetically for 60 min to ensure uniform dispersion, followed by ultrasonication for 90 min using a probe sonicator (400 W, 20 kHz). During preparation, the fluid temperature was maintained below 30°C with an external cooling bath to prevent nanoparticle agglomeration from excessive heating. The stability of the nanofluids was visually monitored immediately after preparation, and sedimentation tests were conducted at 1 and 48 h to confirm homogeneity. Table 1 shows the thermophysical properties of the Fe_3O_4 nanofluid. The nanofluid passes through the bypass valve and is pumped by a small water pump (12 W, 2 L/min, 0.6 m). The pressure gauge and flow meter are connected to this cable as well. A frothy, two-phase flow that travels through the center of the test section is produced by the combination of the nano liquid and air from the injection system entering the test pipe. A gas flow meter measures the air flow rate before it enters the injection system, and a pressure regulator controls the air pressure. A 0.15 mm-diameter nozzle was positioned at the center of the pipe tip's cross-section to allow air bubbles to pass through.

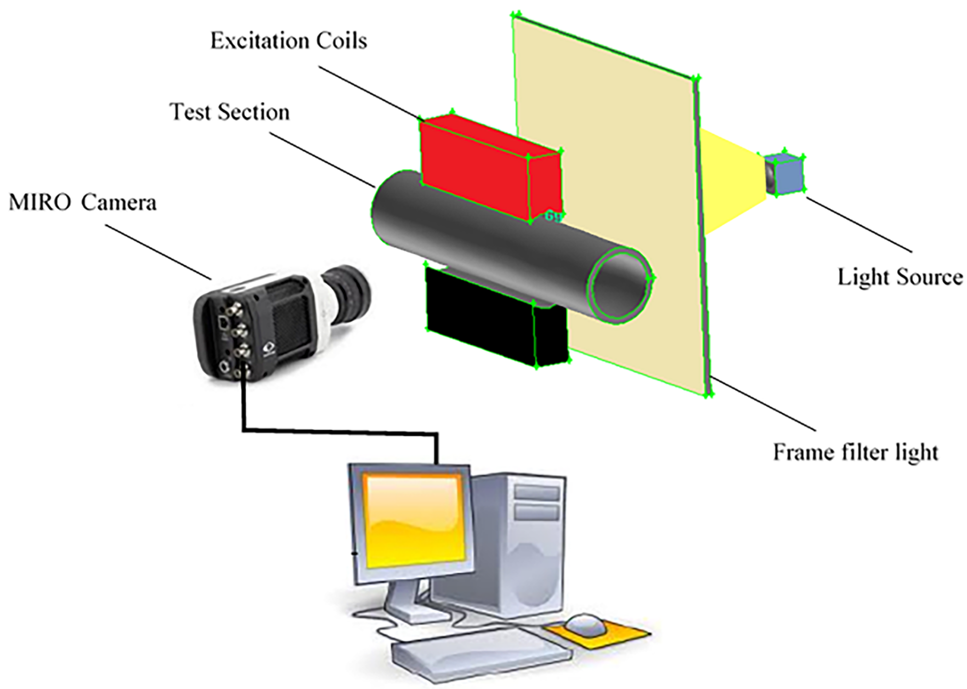

(a) Experimental setup.

Figure 1: (Continued)

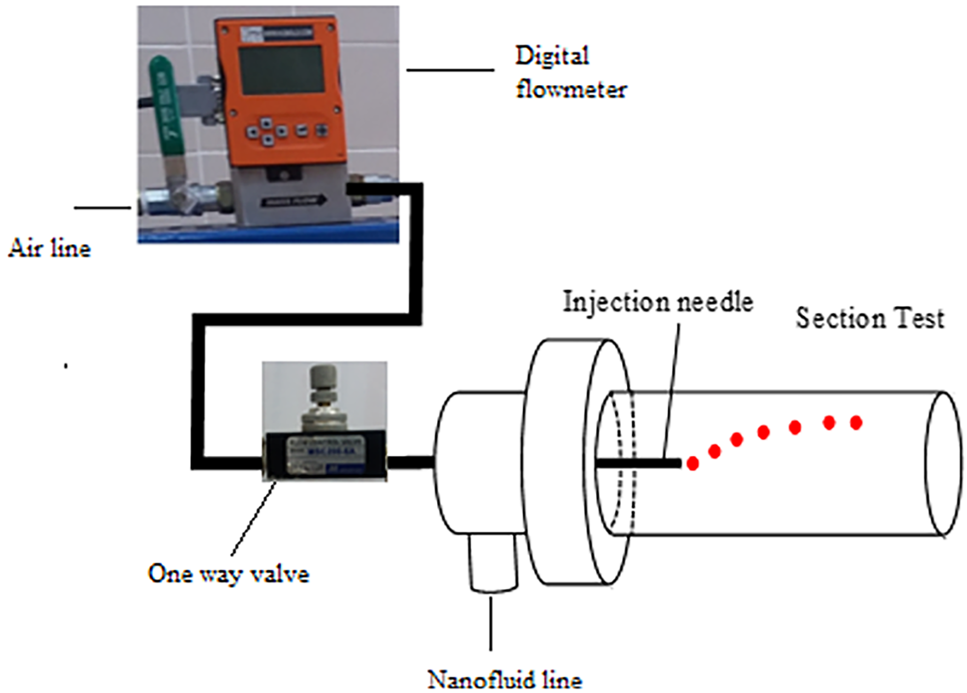

(b) Test section.

Figure 1: The experimental rig and measurement system.

Table 1: Thermophysical properties of the Fe_3O_4 nanofluid [38].

Nanoparticle	Density (kg/m^3)	Thermal Conductivity (W/m·k)	Specific Heat Capacity (J/kg·k)	Electrical Conductivity (S/m)
Fe_3O_4 (50 nm)	5180	8.65	104.2	1×10^5
Nanofluid (water + Fe_3O_4)				
0.5%	1118	0.761	3299.1	31.4×10^{-6}

Using a stopwatch and a tank with a predetermined volume, the flow meter is first calibrated by recording the nanofluid flow rate. As shown in Fig. 1b, the procedure involved filling the tank with 3 L of nanofluid and recording the time required. The flow rate was approximately 4.8 L per minute. The electromagnet, consisting of two coils with 250 wraps of copper wire and a U-type yoke (made of steel), was intended to be charged by a DC source. Between the magnet poles were two sensors from the Tesla meter. The magnetic field between the electromagnet coils was measured over a range of 0 to 4000 gauss.

A frame grabber board, a high-speed camera, a PC, and a lighting system are all part of the image acquisition system. Behind the viewing pipe was a 120-W lamp that provided light. A Phantom Miro digital camera with a maximum resolution of 1280 × 800 was used to take the pictures.

Analysis of uncertainty was an important part of determining the statistical accuracy of the research and experimental data. Through this analysis, potential anomalies in the instrument's calibration can be detected, and the data's inaccuracy can be predicted. To measure the uncertainty, the approach proposed by

Wahhab et al. [21] was used. To find the different errors in measurements as performed in the experiments, the equation shown below was used:

$$W_R = \left[\left(\frac{\partial R}{\partial x_1} w_1\right)^2 + \left(\frac{\partial R}{\partial x_2} w_2\right)^2 + \ldots + \left(\frac{\partial R}{\partial x_n} w_n\right)^2\right]^{0.5} \quad (1)$$

W_R is the uncertainty part, R means the independent variable functionality ($x_1, x_2, \ldots, x_n$), and (w_1, w_2, ..., w_n) is the uncertainty of the independent variables. The accuracy of the air flowmeter was ±0.96%, and its uncertainty was 0.31%. The measurement error of the nanofluid flowmeter was 2.2%. Moreover, magnetic field intensity exhibited an uncertainty of about 2.6% during the experiment. Therefore, the total uncertainty in this experiment was 3.11%.

The influence of the magnetic field was evident by observing the recorded images, as the shape and size of the moving air bubbles changed during the two-phase flow. From the experiments, the air bubbles' shapes, density variations, clear border distributions, and bubble sizes also showed uneven variations from image to image. It was difficult to clearly observe the boundaries of the air bubbles, indicating that using the optical detection method to accurately determine them is challenging. Digital image processing techniques were used to retrieve the data from high-speed video recordings. The MATLAB-based program used three distinct operational steps to process the data: bubble tracking, bubble border identification, and bubble dimension validation. The image processing workflow used in this investigation is shown in Fig. 2. Morphological procedures were employed in the first series to reduce image noise and improve clarity. Each image was converted to a binary image via grayscale thresholding, with threshold values ranging from 0.5 to 0.8 (for interpretation of sensitivity results): the bubble area decreased gradually by approximately 6%–7% as the threshold increased from 0.5 to 0.8; this behavior is expected because higher thresholds eliminate low-intensity edge pixels. The perimeter exhibited only a small reduction (around 5%–6%), indicating stable boundary detection. The shape factor increased slightly with threshold value, suggesting smoother detected bubble contours at higher thresholds. Processing images taken close to the nozzle tip, where bubbles formed, made it harder to identify bubble boundaries. To distinguish the nozzle structure from other image components, the system used an image of the nozzle edge without bubbles (Fig. 2b).

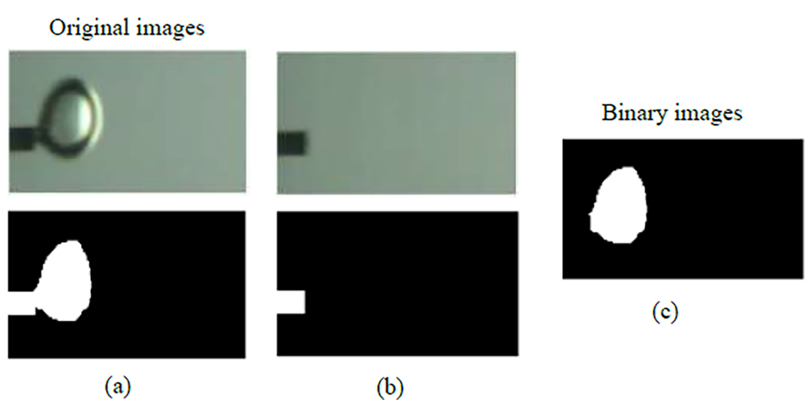

Figure 2: Image processing procedure for a bubble formation; (**a**) original images, (**b**) images without bubbles, and (**c**) binary image.

The algorithm's final step erased the pixels that formed the nozzle contour while matching bubbles in binary images to the reference nozzle image (Fig. 2c). At various magnetic field intensities, the algorithm measured bubbles using their oblate-spheroidal and elliptical interpretations. The equivalent bubble diameter had to be determined under the spherical assumption to simplify calculations.

Inference about Bubble Dimensions

When assessing changes in bubble shape during travel through continuous phases under various external stresses, the shape factor (*SF*) is a crucial measure [21]. A crucial measurement tool for figuring out how bubbles originate and undergo structural changes is the shape factor.

$$SF = \frac{4\pi A}{P^2} \tag{2}$$

where *P* and *A* are the perimeter and the area of the bubble formed, respectively. The value of the bubble shape factor can be determined from zero to one, as it represents a measure of the extent to which the bubble transforms from its elongated ellipse shape (close to zero) to its circular shape (close to one). Based on information provided in the literature, bubbles under flow conditions often appear spherical [25]. In general, the bubbles during formation are approximately elliptical, so the standard shape factor for elliptical bubbles has been adopted. Fig. 3 shows examples of bubbles within the data collection.

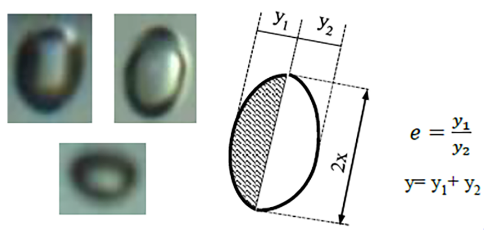

Figure 3: Examples of bubbles within the data collection.

According to the description of Wahhab et al. [21], the mathematical approximation based on Eq. (3) was adopted in calculating the perimeter of the ellipse. Consequently, the symmetrical ellipse's major axis is 2*x*, and its minor axis is *y*. Based on initial computations, this study employs an approximation for elliptical bubbles (e = 0.5) with a margin of error of less than 1.4%.

$$P = \pi\sqrt{2\left(x^2 + y^2\right) - \frac{(x-y)^2}{2.2}} \tag{3}$$

The *SF* elliptical bubble is used as a selection criterion to the extent that the magnetic force affects the bubble shape, while bubble parameters *A* and *P* are functions of the shape factor and aspect ratio *RL* (*RL* = *x*/*y*).

$$SF = \frac{4\pi A}{P^2} = \frac{4xy}{2\left(x^2 + y^2\right) - \frac{(x-y)^2}{2.2}} \tag{4}$$

And,

$$SF = \frac{4\pi A}{P^2}\left[0.2273 + 0.3863\left(RL + \frac{1}{RL}\right)\right] \tag{5}$$

Fig. 4 shows the structure of data implemented in the MATLAB algorithm for this work. The perimeter, area, major axis, and minor axis are the geometric properties of a bubble. Additionally, an analogous diameter is used to calculate the bubble's diameter [25]. These parameters were measured and organized for each bubble in images.

$$d_b = 2\sqrt{\frac{A}{\pi}} \tag{6}$$

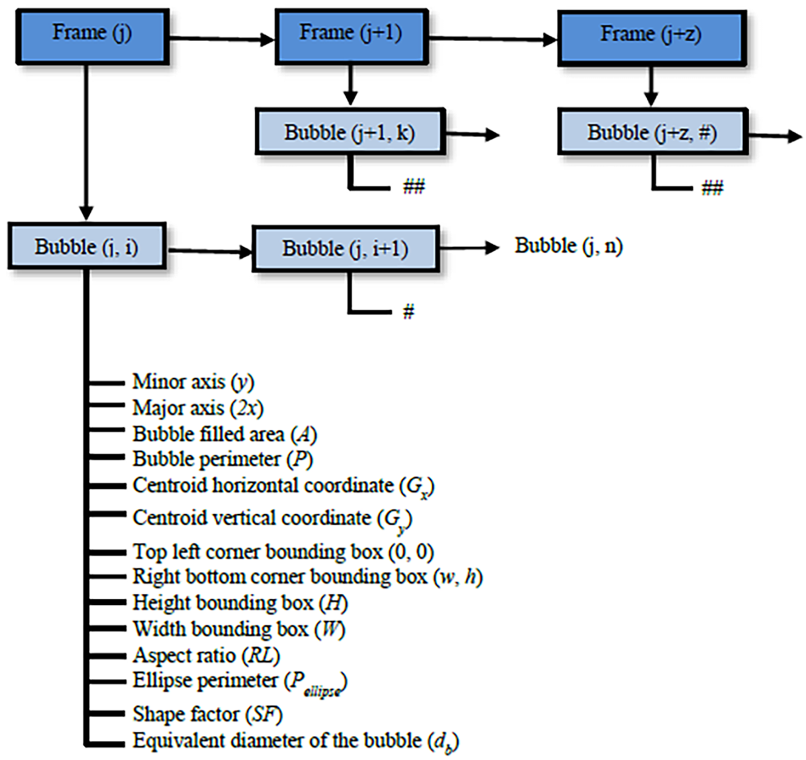

Figure 4: A structured data implementation in a MATLAB algorithm.

3 Numerical Analysis

Computational fluid dynamics (CFD) analysis techniques are efficient tools for modeling mechanical problems and analyzing physical phenomena in engineering applications. In the present simulation, the commercial CFD software ANSYS 19.2 FLUENT MHD Module, with the pre-processing tool SolidWorks 10.0, is used to model and simulate MHD two-phase bubbly flow in a horizontal pipe. This simulation captures the dynamics of air-bubble formation from the mixer nozzle under the influence of a magnetic field. The fluid volume model was used to simulate air bubble formation. The mixer is designed to generate air bubbles in laminar nanofluid flow. The inner diameter of the mixer is 20 mm, and the length of the mixer is 60 mm. Air is injected through the center of the mixer's cross-section via a nozzle. A nozzle diameter of 0.15 mm is used; the mixer's geometrical model is shown in Fig. 5. The unstructured tetrahedral mesh is selected due to the complex geometry. A recommended approach to eliminate the influence of mesh size is to seek a mesh-independent solution; this approach has been followed. The optimal grid size is selected at which the solution is not affected by it. The most accurate and comparable results for bubble formation inside the mixer, bubble velocity, and bubble behavior under a magnetic field were obtained using a fine-meshing scheme, as shown in Fig. 5. Thus, the fine mesh was selected for the simulations and to interpret the results. The number of nodes and elements in the fine mesh was 996,782 and 465,783, respectively.

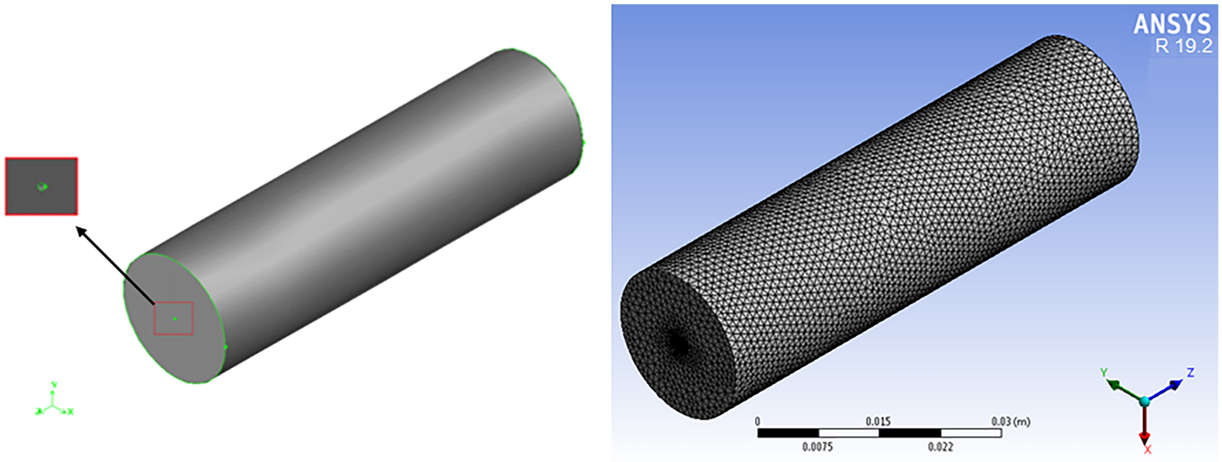

Figure 5: The geometrical model and mesh of the mixer.

Mesh independence: The computational processes were carried out for five selected grid sizes for the MHD model; the summary of the grid independence test results is shown in Fig. 6. Observed that the results of the air volume fraction to bubbly flow produced almost identical results when using nodes 996,782 and 1,245,368. Hence, a domain with 996,782 nodes was chosen to increase computational accuracy and reduce computation time.

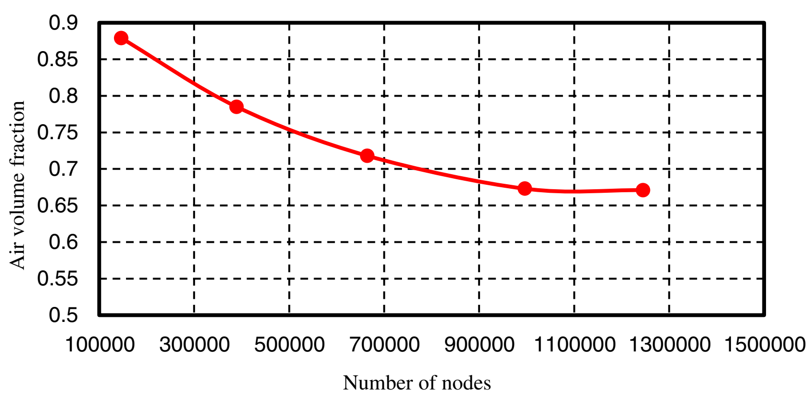

Figure 6: Grid independence test: variation of air volume fraction.

Governing Equations

The solution technique employs the finite volume method to solve the system of governing partial differential equations using the ANSYS 19.2 Fluent MHD Module. A transient numerical simulation of bubble formation in the mixer is carried out using the Volume of Fluid (VOF) method [35]. A few assumptions are made, such as that the fluid is immiscible, incompressible, and Newtonian, and that the flow is laminar. Table 2 shows the boundary conditions for the MHD simulation. Bubble flow dynamics in electrically conductive liquid subjected to an external DC electromagnetic field can be characterized by the following set of equations [22]:

$$\frac{\nabla^2 \vec{B}}{(\mu_o \sigma_l)} + \left(\vec{B}.\nabla\right)\vec{U} - \left(\vec{U}.\nabla\right)\vec{B} = 0 \tag{7}$$

$$\vec{J} = \sigma_l \left(-\nabla \varphi + \left[\vec{U} \times \vec{B} \right] \right) \tag{8}$$

where $\vec{B}$ is magnetic field induction, μ_o—magnetic constant, σ_l—electrical conductivity of liquid, and $\vec{U}$—velocity.

$$\nabla . \vec{U} = 0 \tag{9}$$

$$\frac{\partial \vec{U}}{\partial t} + \left(\vec{U} . \nabla \right) \vec{U} = -\frac{1}{\rho_l} \nabla p + \upsilon_l \nabla^2 \vec{U} + \vec{K} \tag{10}$$

where p—Pressure, ϑ_l—kinematic viscosity, $\vec{K}$—Sum of volume forces, $\vec{K}_{fric} = N\left(\Delta \vec{U}_{\rm lg}\right)/\rho l$—Friction force, $\vec{K}_{Lor} = \left(\vec{J} \times \vec{B}\right)/\rho l$—Lorentz force, $\vec{J}$—Current density, and $\vec{K}_g$—Drag force.

Table 2: Boundary conditions for MHD simulation.

Mixer Unit	
Inlet: the nanofluid and air superficial velocities of 17.78 and 37.3 cm/s, respectively.	
Outlet: Pressure outlet with backflow Tamb.	
Walls: No-slip; interfaces coupled for conjugate heat transfer	
External edges: (a) Top cover, convection to ambient, plus radiation. (b) Back and sides: adiabatic if well insulated.	
Magnetic intensity	1000–4000 gauss
Fe_3O_4 volume concentrations	0.5%

4 Results and Discussion

4.1 Experimental Results

Distinct contrasts in air-bubble forms within nanofluid flow were observed via optical analysis. These contrasts were caused by changes in surface gas and liquid velocities and by an increase in magnetic field intensity, as observed experimentally. When the bubbles' form factor (SF) approached 1.0, it indicated shape stabilization; a circular bubble shape corresponded to this value. On the other hand, an extended elliptical form was suggested by an SF close to zero.

For each test, the imaging procedure recorded at least 700 bubbles. Fig. 7 shows representative air-bubble samples in nanofluid flow. As shown in the figure, the shape factor proved to be a valid metric for assessing how the magnetic field strength affected the bubble's shape stability and deformation behavior.

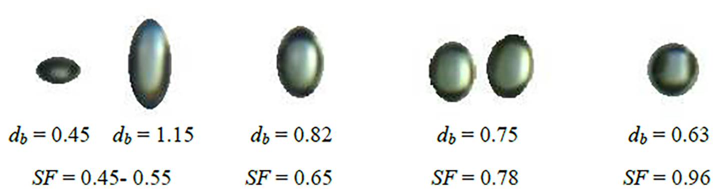

Figure 7: Samples of bubbles under test.

Fig. 8 shows how the bubble form factor changes as magnetic strength increases at surface velocities of 17.78 cm/s for liquids and 37.3 cm/s for gases. For magnetic intensities of 1000, 2000, 3000, and 4000 gauss, respectively, the bubble form factor showed larger ranges within (0.6–0.93), (0.54–0.83), (0.42–0.72), and

(0.36–0.62). According to the results, the elongation of bubbles in nanofluid flow under a magnetic field reduces the bubble form factor with increasing magnetic field intensity.

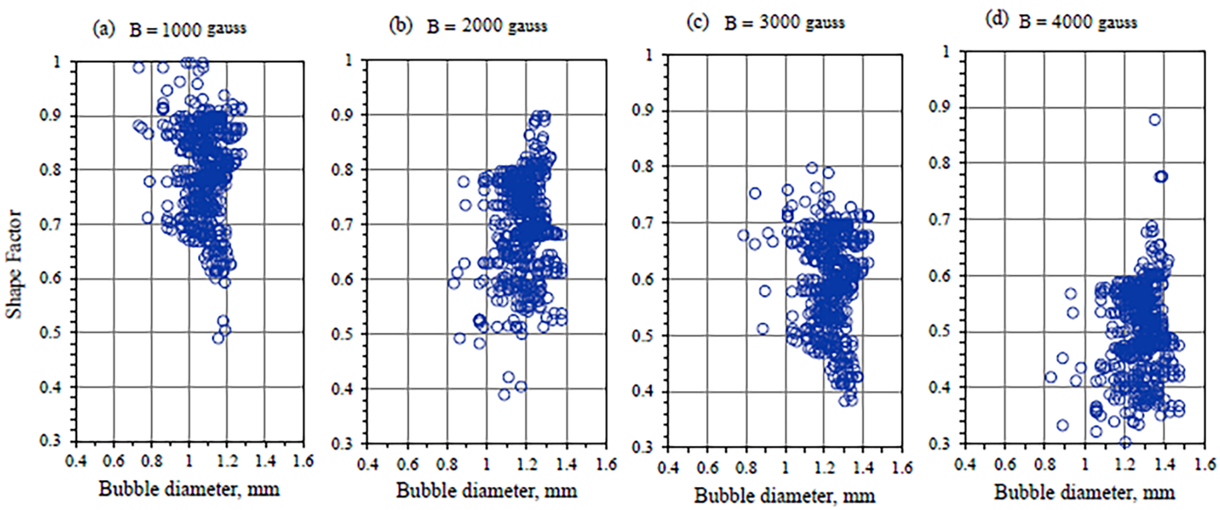

Figure 8: Shape factor values and the effect of magnetic field intensity.

Concurrently, an increase in bubble size is correlated with a decrease in the bubble form factor. The transition of elliptical bubbles to a circular shape during nanofluid flow is slowed by the increased magnetic field, which encourages bubble growth.

As air was injected through a nozzle into a horizontally moving nanofluid channel, air bubbles were observed. Tests were conducted on bubble production from a 0.15 mm-diameter nozzle in nanofluid flow. There were two steps to the bubble expansion from a nozzle edge.

The first stage, when air injects through the nozzle, the air bubble began to growth, with the smaller air bubble size, the buoyancy force is starting to effect on a bubble structure as illustrates in Fig. 9a, this effect is different of what is occurring in the vertical flow, where the buoyancy affect is almost low comparing with a surface tension [39,40]. The bubble appearance at this stage indicated an ellipse, and its major axis was vertical. The second stage is called the bubble elongation stage, so the bubble body is still forming and remains connected to the tip nozzle, where buoyancy increases with bubble size. Moreover, the lift force increases, thereby promoting the buoyant force effect. Fig. 9b shows how the effect of the nanofluid flow causes the primary axis of the elliptical bubble to derail from the vertical axis by generating friction drag and then withdrawing the bubble in the direction of the nanofluid flow [40,41]. Consequently, the bubble will detach from the nozzle tip as this effect progressively develops. Fig. 9c shows the effects that were influenced by the magnetic force and that transpired throughout the bubble expansion. In general, this variation was seen in the rates of bubble formation and the magnetic force produced as the field intensity increased up to 4000 gauss. In the nanofluid phase, the magnetic effect can create a hydrostatic stream in the gas phase, which then begins to affect the orientation of the air bubbles and returns the main axis to the vertical. The bubble elongates towards the major axis during growth to full bubble size, while the liquid/gas interphase is subject to resistance along the minor axis.

Fig. 10 presents a sequence of images showing the formation of successive bubbles under a magnetic intensity of 4000 gauss, where n denotes the order of the air bubbles. The formation process was observed under the influence of the magnetic force, with four consecutive bubbles generated from a 0.15 mm nozzle in nanofluid flow at liquid and gas superficial velocities of 17.78 and 37.3 cm/s, respectively. The experiment was conducted at a magnetic field intensity of 4000 gauss, with no pre-existing bubbles in the system. Table 3 outlines the sequential growth of the four bubbles.

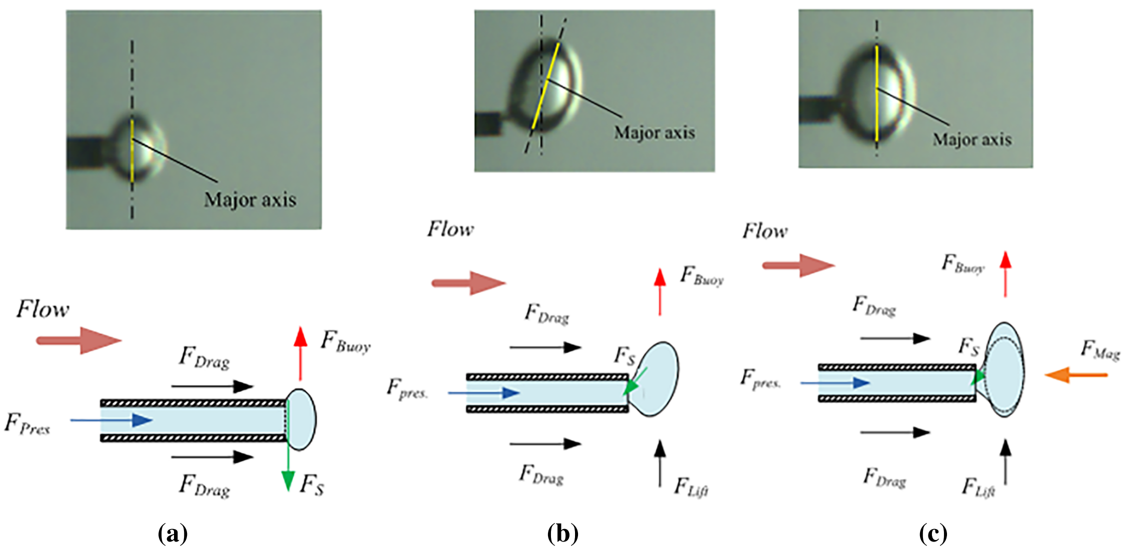

Figure 9: All forces affecting during the bubble growth: (**a**) during starting formation, (**b**) before separating from a nozzle tip, (**c**) with the effect of a magnetic force.

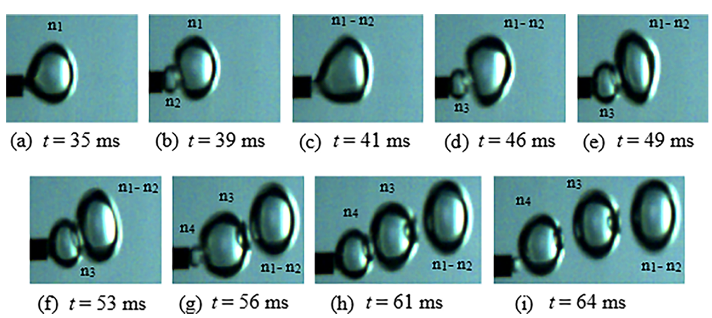

Figure 10: Sequence images of forming four successive bubbles with effective magnetic intensity at 4000 gauss.

Table 3: Successive cases to grow four bubbles consecutively, where n is the order of the bubble.

Image No.	Bubble Order	Growth Time	Remarked
Image (a)	n1	35 ms	The growth of bubble n1 is completed.
Image (b)	n1, n2	39 ms	Bubble n2 in the growth process, because of the bubble place n1, a magnetic force, and the shallow production of an adequate force between n1 and n2.

(Continued)

Table 3 (continued)

Image No.	Bubble Order	Growth Time	Remarked
Image (c)	(n1–n2)	41 ms	Bubbles n1 and n2 merge to train the bubble (n1–n2), the force of the gas pressure for the magnetic force to prevent the movement of n1.
Image (d)	(n1–n2), n3	46 ms	As bubble n3 begins to form, the adhesion force between (n1–n2) and n3 is generated, which causes the main deformation of bubble n3.
Image (e)	(n1–n2), n3	49 ms	The adhesion force between (n1–n2) and n3 is increased by the bubble n3 continuing to develop.
Image (f)	(n1–n2), n3	53 ms	The growth of bubbles (n1–n2) and n3 is completed.
Image (g)	(n1–n2), n3, and n4	56 ms	Bubble n4 is starting to form.
Image (h)	(n1–n2), n3, and n4	61 ms	The continuation of a bubble n4 to grow.
Image (i)	(n1–n2), n3, and n4	64 ms	The growth of bubbles (n1–n2), n3, and n4 is completed.

In the final stage, one of the bubbles (n1–n2) was notably larger than the others, exhibiting a diameter greater than those formed in earlier stages, as illustrated in image (e). This behavior suggests bubble coalescence. The analysis focused on evaluating the impact of magnetic field intensity on the likelihood of coalescence during the formation of successive bubbles.

Following the observation of coalescence between two bubbles and the subsequent increase in the diameter of the bubble (n1–n2), similar data were collected for the formation of successive bubbles under magnetic field intensities up to 4000 gauss. The results indicated that the increase in bubble diameter due to coalescence ranged from 1.2% to 5.5% relative to the original merged bubble diameter. A MATLAB-based image processing algorithm was developed to analyze the growth of successive bubbles at 1000 frames per second, enabling precise measurements of bubble diameters. Fig. 11 illustrates the frequency of bubble diameters over a period of 1060 ms under varying magnetic field intensities: (a) B = 0, (b) B = 1000 gauss, (c) B = 2000 gauss, and (d) B = 4000 gauss. The results revealed that the frequency of larger bubbles resulting from coalescence increased with increasing magnetic field intensity. So, it can be considered that the increase in the magnetic force, caused by the deceleration of the process of bubble growth, is also the same as that caused by the increase in bubble coalescence.

4.2 Numerical Results

To understand the effects of different forces, a numerical simulation was conducted for three cases. In the first case, the 3D simulations were carried out with friction and drag forces included, while the magnetic force was neglected (B = 0). The predicted volume fraction profile showed a peak at the top of the pipe, where air bubbles tend to migrate toward the upper wall. Fig. 12 shows contours of gas volume fraction in the nanofluid flow at B = 0 and during different times: (a) 33 ms, (b) 76 ms, (c) 128 ms, (d) 176 ms.

The simulations were carried out under a magnetic field of B = 1000 gauss. A significant change in behavior was observed in the results: the bubbles tended to migrate upward along the wall, but at B = 1000 gauss, the air bubbles increased in size and expanded vertically in the direction of the continuous-phase flow. Finally, when the magnetic force was increased (i.e., B = 2000 gauss), the air volume fraction profile showed an acceleration of this mechanism, with behavior similar to the vertical elongation of the bubble in the liquid flow, as shown in Fig. 13. These results show good agreement with the experimental and numerical data of Hu et al. [35] for the effect of magnetic force in vertical bubbly flow, and with the data of Abdul-Wahhab et al. [41] on hydrogen bubbles.

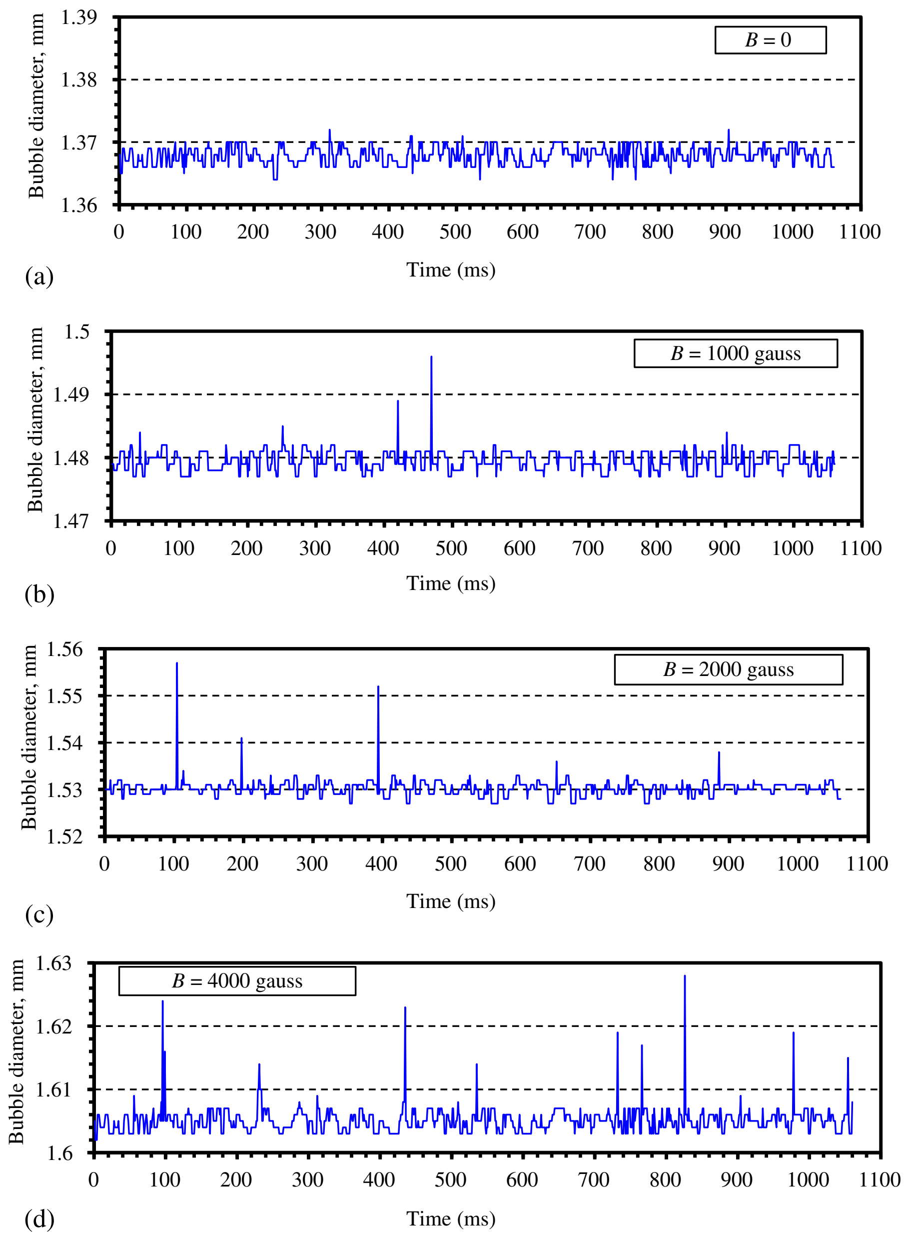

Figure 11: A magnetic field's effect on bubble diameter with time: (**a**) B = 0, (**b**) B = 1000 gauss, (**c**) B = 2000 gauss, and (**d**) B = 4000 gauss.

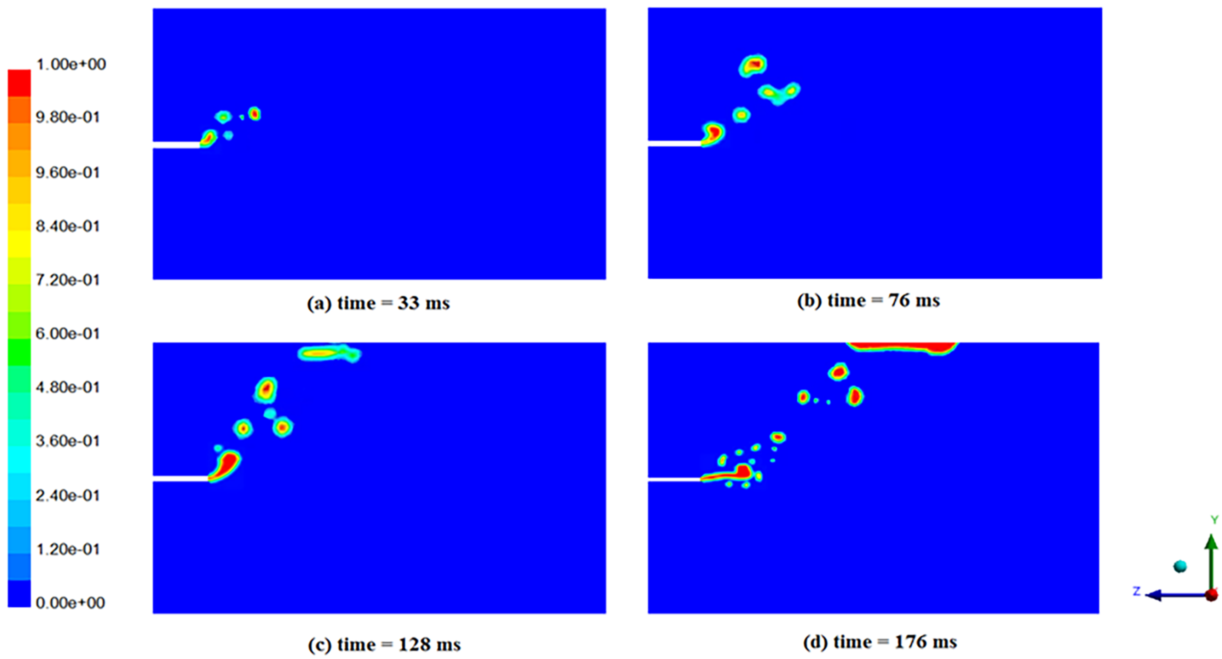

Figure 12: Contours of air volume fraction to bubbly flow at B = 0 and during different times.

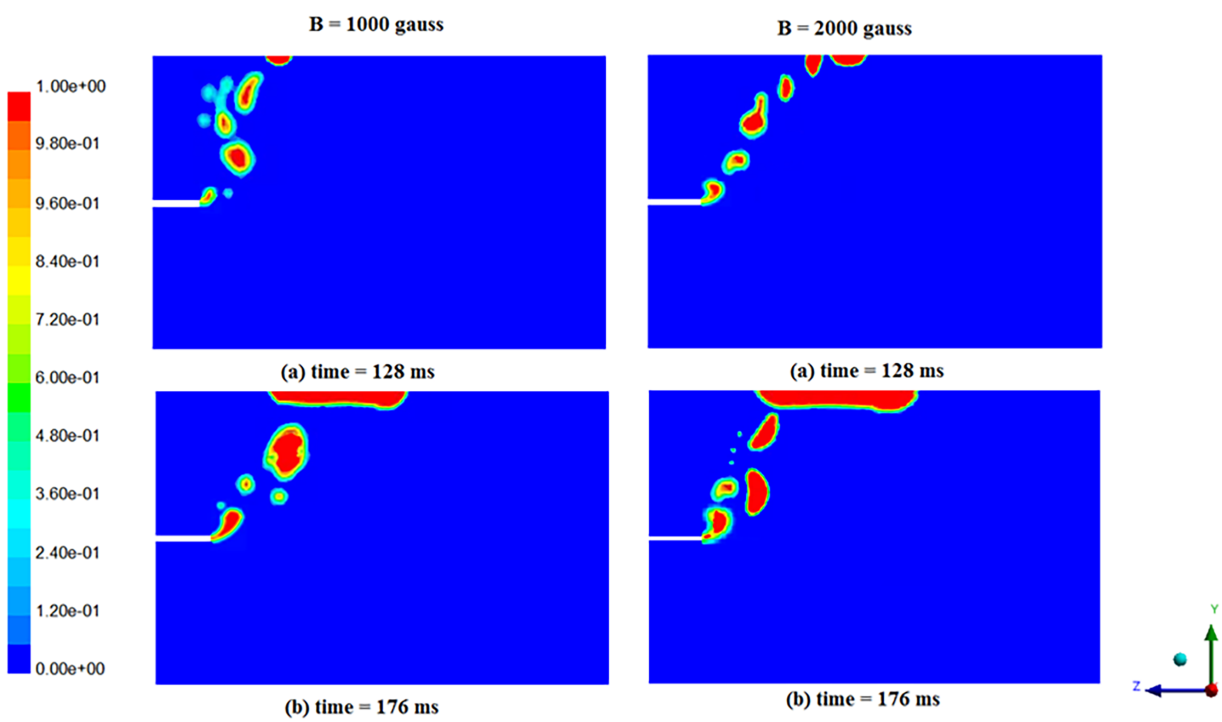

Figure 13: Contours of air volume fraction in nano fluid flow at B = 1000 and 2000 gauss.

4.3 Validation of Numerical and Experimental Results

To validate the numerical model, the predicted bubble dynamics were compared with experimental observations from the high-speed imaging system at different magnetic field intensities. The comparison demonstrated that the numerical simulations successfully reproduced the main experimental trends, including bubble elongation, bubble size increase, upward migration, and the magnetic field's influence on bubble orientation and deformation.

The experimental results showed that increasing the magnetic field intensity reduced the bubble shape factor and promoted vertical elongation and coalescence. Similar behavior was observed in the numerical predictions, where the gas volume fraction contours indicated progressive bubble stretching and enlargement as the magnetic intensity increased from 0 to 2000 gauss. In particular, the numerical model accurately captured the migration of bubbles toward the upper wall at B = 0 and the transition to vertically elongated bubble structures under magnetic-field conditions. Furthermore, the predicted increase in bubble size and the tendency of bubbles to align with the direction of the magnetic force were consistent with the experimental visualization results shown in Figs. 8–11. The numerical simulations also reproduced the experimentally observed delayed bubble detachment and enhanced coalescence at higher magnetic field strengths.

The validation was carried out by comparing the numerical and experimental results for the bubble velocity components of a liquid superficial velocity of 30.6 cm/sec, as shown in Fig. 14. The results show agreement between the numerical and experimental results for the average axial (Ubz) and vertical (Uby) components of bubble velocity, with mean percentage differences of 10.4% and 15.6%, respectively. Fig. 15 shows the comparison results for the average axial velocity of a bubble with an applied magnetic field intensity of 2000 gauss. The mean percentage of differences between them is 12.4%.

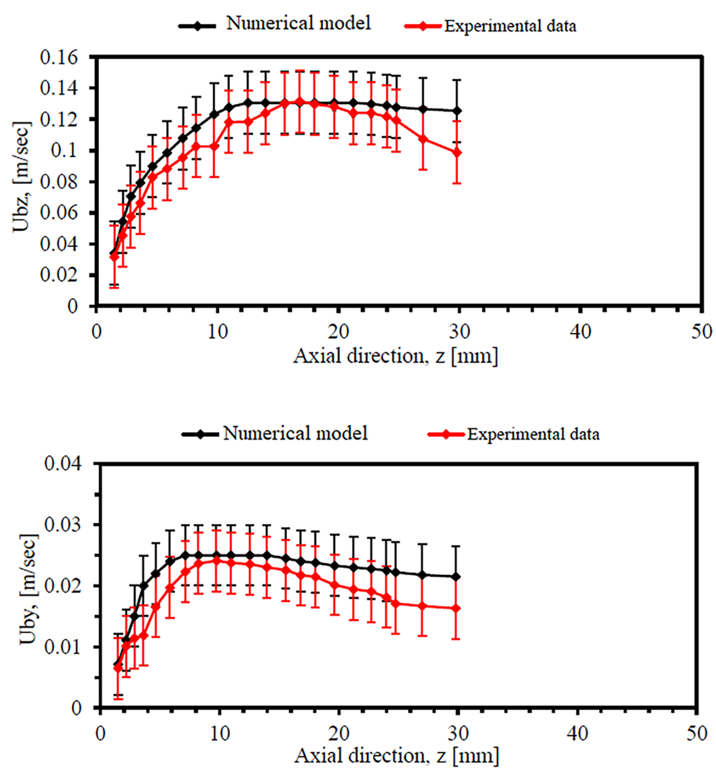

Figure 14: Validation of average axial and vertical components of bubble velocity at magnetic field intensity (B = 0).

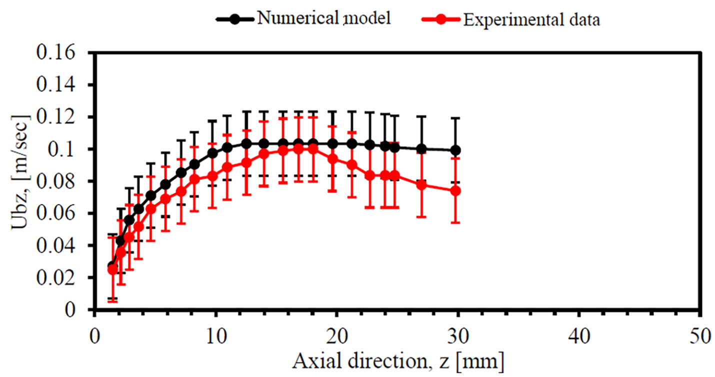

Figure 15: Validation of the average axial component of bubble velocity at magnetic field intensity (B = 2000 gauss).

Overall, the agreement between experimental measurements and numerical predictions was considered satisfactory, with the simulations reproducing the dominant hydrodynamic and magnetohydrodynamic characteristics of the bubbly nanofluid flow. Minor differences between predicted and measured bubble shapes and diameters may be attributed to limitations in turbulence modeling, interface-tracking resolution, and uncertainties in experimental image-processing measurements.

5 Conclusions

Studying magnetohydrodynamics and its impact on bubbly flows, particularly in nanofluids for industrial applications, is important. The current study aims to clarify, using an experimental approach, the extent to which bubbly flow is affected by the magnetic field. An optical monitoring technique is used to investigate the influence of magnetic forces on the growth and formation of air bubbles in horizontal bubbly flow. The main conclusions that have been achieved and drawn are summarized as follows:

- The magnetic field affects the continuous nanofluid phase and therefore influences the gas phase, and the bubbles' features, such as bubble growth process, shape, size, trajectory, and formation velocity. The results showed that, at a magnetic field of up to 4000 gauss and a nanofluid superficial velocity of 17.78 cm/s, the magnetic force had the greatest effect due to the increased electrical conductivity of the nanofluids.
- By applying the magnetic field, up to 4000 gauss on the bubbly nanofluid flow, the diameter of air bubbles formed at the nozzle tip is increased. Results show that the air bubble diameter is increased by 14.0%.
- Also, with the application of a magnetic field, the bubble is delayed in formation, which leads to increased collision and merging of bubbles.
- The magnetic field makes the bubble turbulent and unstable, especially after it separates from the nozzle tip, which appears in its shape and path of movement. While the shape factor of bubbles decreases with increasing magnetic field intensity. This effect is confirmed by the elongation of bubbles within the nanofluid flow.
- The results show agreement between the numerical and experimental results for the average axial and vertical components of bubble velocity, with mean percentage differences of 10.4% and 15.6%, respectively.

As future research, intensify consideration of analytical studies to increase understanding of magnetohydrodynamics by analyzing the mechanisms through which the flow of multi-phase nanofluids can be controlled, and by assessing the extent of the relationship between the multi-phase frictional drag coefficient and the magnetic field intensity. Finally, future investigations should consider three-dimensional numerical modeling for different Reynolds and Hartmann number ranges to improve the prediction accuracy of bubbly nanofluid behavior.

Acknowledgement: The authors acknowledge the University of Technology, Iraq, for supporting the research and for producing this paper.

Funding Statement: The authors received no specific funding for this study.

Author Contributions: The authors confirm contribution to the paper as follows: Conceptualization, Hasanain A. Abdul Wahhab and Hamid Abdallah Dhaher; methodology, Hasanain A. Abdul Wahhab; software, Miqdam T. Chaichan; validation, Saif Ali Kadhim and Hayder Mohsin Ali; formal analysis, Miqdam T. Chaichan; investigation, Muataz S. Alhassan; resources, Mohammed Fathi Muzahem; data curation, Mohammed Fathi Muzahem; writing—original draft preparation, Hasanain A. Abdul Wahhab; writing—review and editing, Miqdam T. Chaichan; visualization, Hamid Abdallah Dhaher; supervision, Miqdam T. Chaichan. All authors reviewed and approved the final version of the manuscript.

Availability of Data and Materials: Data available on request from the authors. The data that support the findings of this study are available from the Corresponding Author, Hasanain A. Abdul Wahhab, upon request.

Ethics Approval: The study do not include human or animal subjects.

Conflicts of Interest: The authors declare no conflicts of interest.

References

1. Soltani M, Kashkooli FM, Fini MA, Gharapetian D, Nathwani J, Dusseault MB. A review of nanotechnology fluid applications in geothermal energy systems. Renew Sustain Energy Rev. 2022;167(3):112729. doi:10.1016/j.rser.2022.112729.
2. Sun L, Geng J, Dong K, Sun Q. The applications and challenges of nanofluids as coolants in data centers: a review. Energies. 2024;17(13):3151. doi:10.3390/en17133151.
3. Ali AH, Ibrahim SI, Jawad QA, Jawad RS, Chaichan MT. Effect of nanomaterial addition on the thermophysical properties of Iraqi paraffin wax. Case Stud Therm Eng. 2019;15(32):100537. doi:10.1016/j.csite.2019.100537.
4. Kazem HA, Al-Waeli AH, Chaichan MT, Sopian K. Numerical and experimental evaluation of nanofluids based photovoltaic/thermal systems in Oman: using silicone-carbide nanoparticles with water-ethylene glycol mixture. Case Stud Therm Eng. 2021;26(3):101009. doi:10.1016/j.csite.2021.101009.
5. Ali AJ, Eddin BE, Chaichan MT. An investigation of effect of hematocrit on thermal conductivity of a bio-nanofluid (MWCNT or SWCNT with blood). Therm Sci Eng Prog. 2021;25(1):100985. doi:10.1016/j.tsep.2021.100985.
6. Wang X, Song Y, Li C, Zhang Y, Ali HM, Sharma S, et al. Nanofluids application in machining: a comprehensive review. Int J Adv Manuf Technol. 2024;131(5–6):3113–64. doi:10.1007/s00170-022-10767-2.
7. Sarafraz MM, Nikkhah V, Madani SA, Jafarian M, Hormozi F. Low-frequency vibration for fouling mitigation and intensification of thermal performance of a plate heat exchanger working with CuO/water nanofluid. Appl Therm Eng. 2017;121:388–99. doi:10.1016/j.applthermaleng.2017.04.083.
8. Chaichan MT, Kazem HA, Al-Ghezi MKS, Al-Waeli AHA, Ali AJ, Sopian K, et al. Effect of different preparation parameters on the stability and thermal conductivity of MWCNT-based Nanofluid used for photovoltaic/thermal cooling. Sustainability. 2023;15(9):7642. doi:10.3390/su15097642.
9. Asadi A, Pourfattah F, Miklós Szilágyi I, Afrand M, Żyła G, Seon Ahn H, et al. Effect of sonication characteristics on stability, thermophysical properties, and heat transfer of nanofluids: a comprehensive review. Ultrason Sonochem. 2019;58(9):104701. doi:10.1016/j.ultsonch.2019.104701.
10. Mohammed HA, Al-aswadi AA, Shuaib NH, Saidur R. Convective heat transfer and fluid flow study over a step using nanofluids: a review. Renew Sustain Energy Rev. 2011;15(6):2921–39. doi:10.1016/j.rser.2011.02.019.

11. Yao Y, Pan Y, Liu S. Power ultrasound and its applications: a state-of-the-art review. Ultrason Sonochem. 2020;62(10):104722. doi:10.1016/j.ultsonch.2019.104722.
12. Oskoui PR, Rezvani M. The Effect of titanium oxide in accelerating the loss rate of magnetic glass ceramics. Next Mater. 2025;9(6):101078. doi:10.2139/ssrn.4826548.
13. Adhikari R, Das S, Das S. Neural networks-based framework for recognizing streaming patterns in magnetized Maxwell-Oldroyd-B blood blended with *Tetra*-hybrid nanoparticles and microbes over stenosis in an elastic artery. Eng Appl Artif Intell. 2024;136:109048.
14. Zhang Y, Tang C, Song Y, Zhang S, Hang ZH, Zhang X, et al. High-entropy alloy nanoparticles combined with an SiC coating synergistically boost the electromagnetic shielding performance of a carbon nanotube sponge. J Mater Chem A. 2024;12(22):13498–509. doi:10.1039/d4ta02088j.
15. Bayareh M, Baghoolizadeh M. An overview of the magnetic field effect on heat transfer and entropy generation in cavities: application of the second law of thermodynamics and artificial intelligence. Int Commun Heat Mass Transf. 2024;151(3):107238. doi:10.1016/j.icheatmasstransfer.2023.107238.
16. Philip J. Magnetic nanofluids (Ferrofluids): recent advances, applications, challenges, and future directions. Adv Colloid Interface Sci. 2023;311:102810. doi:10.1016/j.cis.2022.102810.
17. Kumar A, Dutt N, Awasthi MK, editors. Heat transfer enhancement techniques: thermal performance, optimization and applications. Hoboken, NJ, USA: John Wiley & Sons; 2024.
18. Afrooz IE, Rostami A, Mustaffa Z, Gebretsadik HT. Synergistic effects of electric and magnetic nanoparticles with electromagnetic energy in enhanced oil recovery. Alex Eng J. 2024;98(1):177–86. doi:10.1016/j.aej.2024.04.055.
19. Zhong S, Guo X, Zhou A, Chen ZA, Jin D, Fan M, et al. Fundamentals and recent progress in magnetic field assisted CO_2 capture and conversion. Small. 2024;20(5):2305533. doi:10.1002/smll.202305533.
20. Tawalbeh M, Shomope I, Al-Othman A. Comprehensive review on non-Newtonian nanofluids, preparation, characterization, and applications. Int J Thermofluids. 2024;22:100705. doi:10.1016/j.ijft.2024.100705.
21. Wahhab HAA, Aziz ARA, Al-Kayiem HH, Nasif MS, Afolabi LO. Prediction of the phase distribution of diesel/CNG bubbly flow in a horizontal pipe under the influence of a magnetic field. J Mech Sci Technol. 2017;31(11):5299–309. doi:10.1007/s12206-017-1024-1.
22. Jiang H, Wang X, Ding C, Shan D, Guo B, Qi H, et al. A review of emerging design and theoretical progress on vapor chamber for efficient thermal performance. Int J Heat Mass Transf. 2024;231:125814. doi:10.1016/j.ijheatmasstransfer.2024.125814.
23. Li H, Zhuang Y, Feng JC. Multi-scale experimental analysis on the coupled effects of ultrasonic field and magnetic field on the melting and energy storage performances for hybrid nano-enhanced phase change materials. J Energy Storage. 2024;84(1):110801. doi:10.1016/j.est.2024.110801.
24. Benam BP, Mohammadilooey M, Sadaghiani AK, Çakır E, Acar HY, Park HS, et al. On saturated flow boiling heat transfer of deionized water/ferrofluid on structured surfaces with or without external magnetic field. Int J Heat Mass Transf. 2025;236:126323. doi:10.11159/enfht23.178.
25. Abdul Wahhab HA, Petronas UT, Aziz ARA, Petronas UT, Al-Kayiem HH, Petronas UT, et al. Mathematical modeling of the flow of diesel-CNG fuel mixture in a pipe under the influence of a magnetic field. J Appl Fluid Mech. 2017;10(1):389–96. doi:10.18869/acadpub.jafm.73.238.26293.
26. Preso DB, Fuster D, Sieber AB, Obreschkow D, Farhat M. Vapor compression and energy dissipation in a collapsing laser-induced bubble. Phys Fluids. 2024;36(3):033342. doi:10.1063/5.0200361.
27. Mofrad YM, Asiaei S, Shaygani H, Salehi SS. Investigating the effect of magnetic field and nanoparticles characteristics in the treatment of glioblastoma by magnetic hyperthermia method: an *in silico* study. Results Eng. 2024;23(1):102473. doi:10.1016/j.rineng.2024.102473.
28. Abu-Nab AK, Mamdouh HO, Mohamed KG, Abu-Bakr AF. Hydrodynamics and heat transfer of cavitation bubble in nanoparticles/water nanofluids based on the effects of variable surface tension and viscous forces. J Nanofluids. 2023;12(8):2044–55. doi:10.1166/jon.2023.2067.
29. He X, Song X, Peng H, Huang W, Zhang J. Heat flux characteristics during growth and collapse of wall-attached cavitation bubbles with different wall wettability: a lattice Boltzmann study. Ocean Eng. 2023;276:114261. doi:10.1016/j.oceaneng.2023.114261.

30. Zhang X, Fan Z, Cai L, Fu Y, Liu J, Tong Q, et al. Instability and collapse mechanisms of O_2 and N_2 nanobubble gas-liquid interfaces: a molecular dynamics simulation study. Phys Fluids. 2024;36(12):122003. doi:10.1063/5.0242905.
31. Sagar HJ, el Moctar O. Hydroelasticity effects induced by a single cavitation bubble collapse. J Fluids Struct. 2024;127:104131. doi:10.2139/ssrn.4689749.
32. He X, Peng H. Modeling inception and evolution of near-wall vapor thermo-cavitation bubbles via a lattice Boltzmann method. Int J Hydrog Energy. 2024;49:828–49. doi:10.1016/j.ijhydene.2023.09.092.
33. Thesiya D, Patel H, Patange GS. A comprehensive review electronic cooling: a nanomaterial perspective. Int J Thermofluids. 2023;19(1):100382. doi:10.1016/j.ijft.2023.100382.
34. Wahhab HAA, Aziz ARA, Al-Kayiem HH, Nasif MS, El-Adawy M. Magneto-hydrodynamics of bubbly flow in horizontal pipe: new criteria through numerical simulation. AIP Conf Proc. 2018;2035:070002.
35. Hu J, Yang C, Zhang Y, Song H, Lu M, Meng Z, et al. Effect of bubble volume on the sweeping velocity of air bubbles in horizontal pipelines in water supply system. Front Earth Sci. 2023;11:1214713. doi:10.3389/feart.2023.1214713.
36. Wang ZM, Zhang J. Corrosion of multiphase flow pipelines: the impact of crude oil. Corros Rev. 2016;34 (1–2):17–40. doi:10.1515/corrrev-2015-0053.
37. Zhong Y, Zhao Y, Gao X, Bao F. Experimental study on interaction between a cavitation bubble and an oil layer-water interface. AIP Adv. 2024;14(6):065113. doi:10.1063/5.0211208.
38. Gal S, Cabaleiro D, Hassen W, Rault L, Ba H, Estellé P. Surface tension of graphene/Fe_3O_4 water-based hybrid nanofluids. J Mol Liq. 2025;417(2):126630. doi:10.1016/j.molliq.2024.126630.
39. Hsu CC, Chiu YH, Tsai FT, Chou SH, Sheng LT. The effects of magnetic field control on the aggregation of magnetic particles on the heating surface during pool boiling. Int Commun Heat Mass Transf. 2024;152(7):107289. doi:10.1016/j.icheatmasstransfer.2024.107289.
40. Peng H, Fei L, He X, Carmeliet J, Churakov SV, Prasianakis NI. Three-dimensional modelling of cavitation bubble collapse using non-orthogonal multiple-relaxation-time lattice Boltzmann method. Ocean Eng. 2024;294:116720. doi:10.1016/j.oceaneng.2024.116720.
41. Abdul-Wahhab HA, Aziz ARA, Al-Kayiem HH, Nasif MS. Modeling of diesel/CNG mixing in a pre-injection chamber. IOP Conf Ser Mater Sci Eng. 2015;100:012044.